RSC Advances

PAPER

View Article Online
View Journal | View Issue

Cite this: *RSC Adv.*, 2026, **16**, 7447

Engineering the electronic structure towards enhanced performances of CO_2 adsorption and conversion of a Ti-doped MoS_2 monolayer: a DFT study

Junbo Wang,[a] Qiankai Zhang,[b] Qi Tang,[a] Yin Zhang,[a] Jun Zhou,[b] Yang Wang*[c] and Kai Wu[b]

The active site of MoS_2, predominantly located at the crystalline edge, limits selectivity for the CO_2 reduction reaction (CO_2RR). Single-Atom Catalysts (SACs), have emerged as a promising avenue to enhance the catalytic performance of MoS_2, owing to their high catalytic selectivity on the basal plane and tunable activity in various chemical reactions. In this regard, transition metals from the 8B and 1B groups (Cr, Cu, Sc, Ti, V, and Ni) were investigated as dopants on the basal plane for the first time, employing first-principles calculations based on a 4 × 4 × 1 supercell of the MoS_2 monolayer. The Ti/MoS_2 catalyst was identified as the most stable among the SACs, attributed to its optimal formation energy. Various Ti-doped models were analyzed, encompassing energy band structure, density of states, charge differential density, Bader charge, and Gibbs free energy. Our findings indicate that Ti induces diminished electron binding, thereby weakening C=O with lower energy, consequently enhancing the availability of surface sites and facilitating catalytic reactions. In our investigation of possible reaction pathways, the preferred CO_2RR pathway was identified as the reverse water gas conversion (RWGS), with the rate-limiting step being CO_2 hydrogenation into carboxyl (*COOH). The Ti modification model on the MoS_2 basal surface demonstrated exceptional catalytic performance, reducing the rate-limiting step to 0.177 eV, which is 17 times lower than that of pure MoS_2. These calculational results provide valuable theoretical insights for designing highly efficient SACs on MoS_2-based functional materials.

Received 20th October 2025
Accepted 20th January 2026

DOI: 10.1039/d5ra08046k

rsc.li/rsc-advances

1 Introduction

The escalating emission of greenhouse gases (GHGs) has led to significant detrimental effects on Earth's climate systems, driving urgent demand for efficient CO_2 capture and conversion technologies.[1] This urgency has catalyzed the development of advanced carbon capture and utilization (CCU) technologies, among which the CO_2 reduction reaction (CO_2RR) stands out for its dual capacity to mitigate emissions and generate value-added carbon-based products (*e.g.*, CH_4, CH_3OH).[2] Central to CO_2RR efficiency is the intricate interplay between CO_2 adsorption energetics and intermediate desorption kinetics on catalyst surfaces—a dynamic process governed by the modulation of electronic structure and atomic-scale site specificity.[3–5]

Two-dimensional (2D) transition metal dichalcogenides (TMDs), particularly molybdenum disulfide (MoS_2), have emerged as versatile platforms for CO_2RR due to their tunable band structures (1.2–1.9 eV), layer-dependent conductivity, and propensity for defect engineering.[6–9] Unlike graphene's homogeneous π-electron system, the anisotropic d-orbital configuration of MoS_2 enables selective activation of CO_2's degenerate molecular orbitals.[10] However, intrinsic limitations persist: the basal plane exhibits weak CO_2 physisorption (E_{ads} < 0.3 eV), while catalytically active edge sites constitute <5% surface coverage in conventional synthesis.[11,12]

To overcome the limitations of pristine MoS_2 in CO_2 reduction, chemical doping has emerged as an effective strategy to reconfigure its electronic structure and unlock new catalytic functionalities. Noble metals (*e.g.*, Au, Pt, Pd, Ag) reduce the bandgap and facilitate charge transfer, while transition metals (TMs) such as Cu, Fe, and Ni introduce localized electronic states near the Fermi level, enabling direct interaction with CO_2's antibonding orbitals and modulating the d-band center.[13–15] These dopants not only enhance CO_2 chemisorption but also reshape intermediate binding energies. For instance, Cu doping increases CO_2 adsorption by up to 200%, attributed to synergistic surface area expansion and charge redistribution.[16] Fe dopants, *via* Fe 3d–C 2p orbital

[a]*Foshan Power Supply Bureau of Guangdong Power Grid, Foshan 528000, China*
[b]*Institute of Science and Education Development, Xi'an Jiaotong University, 28 Xianning West Road, Xi'an 710049, China*
[c]*School of Electronics and Information, Xi'an Polytechnic University, 19 Jinhua South Road, Xi'an 710048, China. E-mail: wangyang@xpu.edu.cn*

hybridization, weaken the C=O bond, achieving $\Delta E_{ads} \approx -1.2$ eV.[17] Furthermore, Ni-doped MoS_2 demonstrates altered spin polarization and charge transfer dynamics that influence catalytic selectivity.[18] *In situ* spectroscopic studies reveal that even minor shifts in charge density ($\Delta\rho < 0.1$ $e^- Å^{-3}$) at active sites can lead to over 50% changes in product selectivity, highlighting the catalytic sensitivity to local electronic environments.[19] In addition, a recent systematic investigation demonstrated that substitutional doping at both Mo and S sites strongly modulates the work function of MoS_2, with Ti and Nb identified as the most effective dopants for enhancing electronic responsiveness.[20]

Despite these advances, balancing CO_2 adsorption with controlled CO desorption remains a persistent challenge that limits catalyst performance and product selectivity. While reduced energy barriers for CO_2 activation are often desirable, excessively facile *CO desorption can hinder further reduction steps, resulting in accumulation of CO as a by-product. Lv *et al.*[21] showed that doped MoS_2 structures with enhanced surface charge densities lower reaction barriers, yet compromise *CO retention required for deeper reduction. Similarly, vertical Nb-doping reported by Abbasi *et al.* promotes CO desorption but restricts C–C coupling pathways.[22] Conversely, strategies aimed at increasing *CO desorption barriers—such as transition metal doping designed by Li *et al.*—successfully suppress CO evolution, enabling longer cascade reactions.[23] These findings underscore the importance of fine-tuning *CO binding energies to balance catalytic activity and selectivity. However, most existing studies focus on isolated descriptors (*e.g.*, adsorption energy or conversion), without a holistic view of how dopant characteristics simultaneously influence both CO_2 capture and conversion steps.

To address this critical gap, we employ first-principles density functional theory (DFT) to systematically evaluate a set of transition metal dopants (Cr, Cu, Sc, Ti, V, Ni) in MoS_2, targeting dual-functionality in CO_2 reduction. Among these, Ti emerges as the most promising candidate, offering the lowest formation energy and a favorable electronic environment for CO_2 activation. We conduct a comprehensive comparison of three distinct Ti doping configurations—sulfur substitution, molybdenum substitution, and interlayer intercalation[24,25]—revealing clear structure–function relationships among dopant positioning, Bader charge transfer, and activation barriers. Furthermore, our detailed reaction pathway analysis elucidates the CO_2-to-CO conversion mechanism on Ti/MoS_2, identifying rate-limiting steps and quantifying *CO desorption energetics. Our study offers a unified design framework that links dopant physicochemical properties with catalytic performance, providing critical insights for the development of next-generation MoS_2-based CO_2RR catalysts with optimized capture–conversion synergy.

2 Computional approach

In order to ensure the simulation was sufficiently large that an adsorbed gas molecule was not affected by nearby gas molecules, a periodic ($4 \times 4 \times 1$) supercell of the MoS_2 monolayer was modelled. The MoS_2 monolayer was composed of 16 Mo and 32 S atoms.[26] It should be noted that to avoid interlayer interactions, a vacuum layer of 15 Å was constructed in the direction from the interface to the isolated slab boundary condition.

We conducted all calculations using CASTEP on the DFT theory plane-wave pseudopotential method for exploring the electronic and structural properties.[27] Electronic interaction energies were computed employing the generalized gradient approximation (GGA) functional and the Perdew–Burke–Ernzerhof (PBE) functional.[28] Here, the cutoff energy was set to be 500 eV, and the *k*-point grids used were $6 \times 6 \times 1$.[29] We set the convergence criteria for the optimization of energy, remaining stress, and force to be 0.01 meV per atom, 0.05 GPa, and 0.01 eV $Å^{-1}$, respectively.[30] The long-range dispersion correction (DFT-D2) method, proposed by Grimme, was selected to modify the effects of the van der Waals interactions in all the constructed models.[31,32] The total energy was converged to <10 meV. All calculations were performed using the same relaxation criteria.

The validity of the calculation can be established by comparing the formation energy of the M-doping model. The formation energy (E_f) served as a metric to evaluate the feasibility of dopant integration and the stability of the doped system within the lattice, as outlined in eqn (1):[33]

$$E_f = \left(E_{doped} - \sum n_{doped}\mu_{doped}\right) - \left(E_{pure} - \sum n_{superseded}\mu_{superseded}\right) \quad (1)$$

where E_{doped} and E_{pure} are the total energy of doped and pure MoS_2 models, respectively. n_{doped} and $n_{superseded}$ represent the number of doped and superseded elements. μ_{doped} and $\mu_{superseded}$ refer to the chemical potential of doped and superseded elements. For metal elements, μ_{Mo}, μ_{Cr}, μ_{Cu}, μ_{Sc}, μ_{Ti}, μ_V, and μ_{Ni} were defined as the total energy of metal divided by the number of atoms in bulk. For non-metallic elements, μ_S was obtained by putting the most stable element in a 10 Å × 10 Å × 10 Å cube box, respectively.

In terms of adsorption energy, the greater the absolute value of adsorption energy on the surface, the better the adsorption performance of CO_2. The formula is as follows:

$$E_{ads} = E_{gas+surface} - E_{gas} - E_{surface} \quad (2)$$

where $E_{gas+surface}$ and E_{gas} are the calculated energies of the model after adsorption of the CO_2 on the surface and the free CO_2 molecule, respectively.

3 Results and discussion

3.1 Properties of Ti-doped MoS_2 monolayer

To identify suitable dopants for MoS_2 in CO_2 hydrogenation, we focused on 3d transition metals (Cr, Cu, Sc, Ti, V, and Ni) due to their propensity to modulate the electronic structure of the host catalyst. The practical feasibility of doping hinges critically on the thermodynamic stability of the doped structure. Therefore, we first computed the formation energy (E_f) for each candidate,

Table 1 Formation energy of M1/MoS_2

Dopant	Formation energy (eV)	Dopant	Formation energy (eV)
Cr	−3.45	Ti	−3.93
Cu	−0.29	V	−3.88
Sc	−2.54	Ni	−2.27

as presented in Table 1. Among them, Ti doping exhibits the most negative formation energy, indicating its most stable incorporation into the MoS_2 lattice.

Although V and Cr also show reasonably low formation energies, the difference from Ti remains sufficient to suggest that Ti is the most thermodynamically favorable dopant under comparable conditions. For this reason—and to allow a focused mechanistic analysis—we selected Ti as the representative dopant for detailed electronic, adsorption, and reaction-pathway investigations. This computational selection aligns with and provides a theoretical foundation for experimental observations of Ti's enhanced catalytic performance.[34–36] The comparative study of other dopants with similar stability (*e.g.*, V, Cr) is considered an interesting direction for future work. Fig. 1(a) depicts the relaxed structure of MoS_2 obtained in this study, while Fig. 1(b–d) illustrates the Ti-doped and decorated structures. Overall, the influence of doping and decorating on the MoS_2 structure was observed to be minimal. Doping agents remain centered between neighboring atoms, and the positions of Mo and S atoms within the structure exhibit minor changes. The calculated Mo–S bond length and Mo–Mo distance in pristine MoS_2 were determined to be 2.400 Å and 3.167 Å, respectively, and were consistent with theoretical data (2.420 Å and 3.190 Å).[37,38] Additionally, the angle of the S–Mo–S bonds in the optimized pure MoS_2 was calculated to be 82.548°, showing reasonable agreement with theoretical and experimental data.[39–41] In this regard, the calculation method and parameters used for modeling MoS_2 were appropriate. Table 2 reveals that the E_f values for all Ti-doped MoS_2 surfaces are negative, indicating an exothermic process. We considered all potential sites on the basal plane. In this context, 1Ti-MoS_2 denotes MoS_2 with a Ti atom substituting for a Mo atom, 2Ti-MoS_2 represents MoS_2 with a Ti atom replacing an S atom, and

Table 2 Structure formation energy and atomic details of different doping sites. (Δ_{Ti-X} represent the distance between the Ti atom and its nearest neighbor atom; $\theta_{O=C=O}$ is the angle between the Ti atom and its two nearest neighbors)

Structure	E_f, eV	Δ_{Ti-X}, Å	$\theta_{X=Ti=X}$, °
MoS_2	*	*	*
1Ti-MoS_2	−9.15	2.415	83.718
2Ti-MoS_2	−3.93	2.611	73.609
3Ti-MoS_2	−3.81	2.319	89.510

3Ti-MoS_2 signifies MoS_2 with a single Ti atom modifying the surface. Among them, given the comparable ionic radii of Ti^{4+} and Mo^{6+}, the incorporation of Ti dopant into the lattice induced subtle deviations in the lattice parameters; nevertheless, the observed alterations were deemed negligible in magnitude. In contrast, 2Ti-MoS_2 and 3Ti-MoS_2 are challenging to synthesize compared to 1Ti-MoS_2, owing to differences in ionic radius and doping site. However, overall, they still provide indications of thermodynamic stability.

It is important to clarify the purpose of studying these less-favorable configurations: they are not presented as the most readily synthesizable structures, but as critical models to elucidate the structure–property relationship. The comparative analysis of 1Ti, 2Ti, and 3Ti-MoS_2 allows us to isolate the effect of Ti coordination environment—from fully coordinated lattice substitution to under-coordinated surface sites—on the electronic structure and catalytic activity.

To unveil the electronic structure changes in doped MoS_2 on the basal plane, DFT calculations were conducted for pure MoS_2 and three distinct doping systems at various sites. Fig. 2 shows the band structure and partial density of states (PDOS) of all the models. The results indicate that the band gap of pure MoS_2 is 1.735 eV, consistent and reliable compared to previous calculations.[42]

Additionally, Fig. 2(b) illustrates that the Mo 4d and S 3p states constitute the conduction and valence bands of pure MoS_2, respectively. In the case of 1Ti-MoS_2, the Ti 3d state exhibits a slight peak change in the band gap, as depicted in Fig. 2(c and d). Despite Ti replacing Mo, the system undergoes insignificant changes due to the similar atomic radius and the

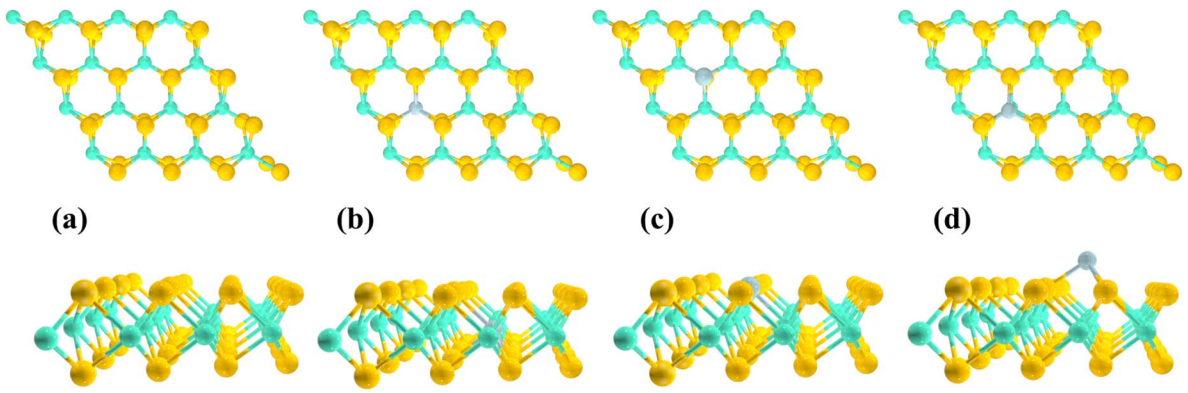

Fig. 1 (a) The top and side views of the optimized pure MoS_2 monolayer, (b and c) the MoS_2 monolayer doped with one Ti atom, and (d) the MoS_2 monolayer decorated with one Ti atom. Here, the light green, yellow, and gray circles represent Mo, S, and Ti atoms, respectively.

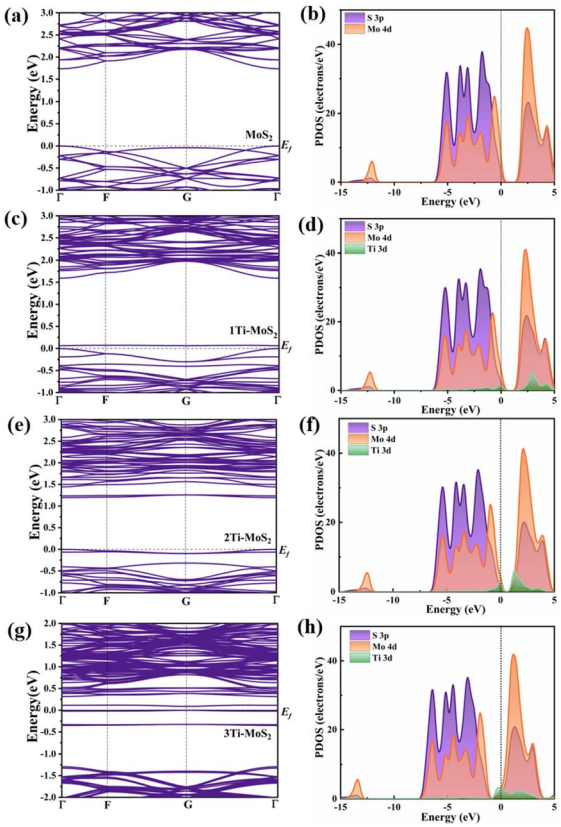

Fig. 2 Band structure and PDOS of (a and b) MoS_2; (c and d) 1Ti-MoS_2; (e and f) 2Ti-MoS_2; (g and h) 3Ti-MoS_2. The dash lines are Fermi level. The energy is referenced to the Fermi level (E_f), which is indicated by the dashed line at 0 eV.

same number of valence electrons. The Mo 4d state and Ti 3d state exhibit a consistent trend above the Fermi level and effectively overlap with the S 3p state, demonstrating a stable bonding effect. In comparison to 1Ti-MoS_2, the Ti state effect in 2Ti-MoS_2 is more pronounced. Due to the substitution at the S-site, Ti introduces additional electrons in the model, represented as the donor level.

As depicted in Fig. 2(e), noticeable isolated energy levels appear. Fig. 2(f) corresponds to the contribution of the Ti 3d state, where influences the bottom of the conduction band, concurrently reducing the overall band gap to 1.196 eV, a value similar to the other theoretically calculated one.[43] In contrast to the empty band in 1Ti-MoS_2, these filled electrons can more effectively facilitate electron participation in surface CO_2 adsorption and catalytic conversion. Among these, the peak coincidence between Ti 3d and the other two states in PDOS is reduced, suggesting that alternative sites in 2Ti-MoS_2 may weaken the bonding ability with surrounding atoms, potentially leading to lattice distortion in the model. Besides, from Fig. 2(g and h), Ti doping on the surface significantly influences the energy band, introducing multiple impurity levels within the band gap. This facilitates easier electron transition to surface reactions. The PDOS diagram also illustrates that doping causes a leftward shift in the overall band edge, with Ti 3d states comprising the majority of the impurity levels.[24] In contrast to the previous calculation model, the Ti 3d state in PDOS and its binding ability with the surrounding S atoms is not as strong as in 1Ti-MoS_2.

Combining the band structure and PDOS analysis, it can be concluded that the introduction of impurity energy levels into the model through Ti doping facilitates the migration of carriers and improves catalytic activity. Moreover, with the different doping sites, the electron density differences and Bader charge were calculated to explore the influence of doping on charge transfer and interaction. The difference in electron density between pure MoS_2, 1Ti-MoS_2, 2Ti-MoS_2 and 3Ti-MoS_2 is represented in Fig. 3. From Fig. 3(a), it can be clearly seen that Mo and S gain and lose electrons in the model. In line with the electronic structure results in Fig. 2(c and d), there is no noticeable change in the gain and loss of electrons after Ti substitutes for Mo atoms, and the electrons remain relatively stable. Similarly, in the 2Ti-MoS_2 model, the relatively large atomic radius of Ti and the additional electron contribution result in a slightly distorted optimized model, leading to the appearance of impurity levels. The substitution of Ti at the S site introduces extra electrons on the surface, enhancing their involvement in reactions. This phenomenon is likely to be advantageous for CO_2 adsorption and subsequent catalytic conversion reactions.

In the 3Ti-MoS_2 model, the charge density difference reveals substantial electron accumulation around the Ti sites, indicating that Ti introduces additional surface-active electrons capable of strengthening CO_2 adsorption and facilitating its subsequent activation. Meanwhile, the structural deformation after Ti incorporation remains minimal, allowing the reaction to occur on a geometrically stable surface. Combined with the reduced band gap and enhanced charge redistribution observed in the 2Ti-MoS_2 and 3Ti-MoS_2 models, these features collectively

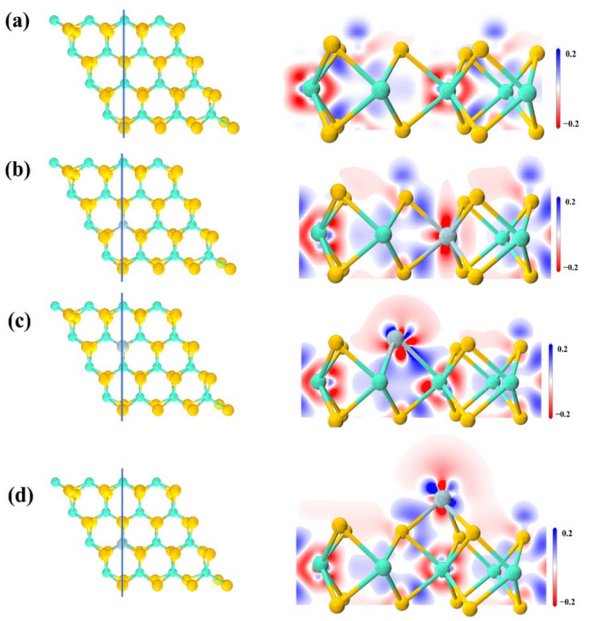

Fig. 3 The line in the figure represents the location of the slice of the electron density difference plot. Electron density difference: (a) MoS_2; (b) 1Ti-MoS_2; (c) 2Ti-MoS_2; (d) 3Ti-MoS_2. The isovalue is set to 0.2 e $Å^{-3}$.

contribute to more efficient catalytic behavior. Notably, these trends are consistent with the recent systematic doping study,[20] which also identified Ti as one of the most effective dopants for tuning the electronic structure and reactivity of MoS_2.

In this regard, we meticulously calculated the Bader net atomic charge of each atom in all structures in order to determine an atom's charge state quantitatively by comparing its calculated charge with its own valence charge. Table 3 outlines the range of variation in Bader charge for different doping configurations. Within pure MoS_2, the S atom exhibits an acquired electron state, while the Mo atom experiences electron loss. In 1Ti-MoS_2, some S atoms gain additional electrons, indicating a relative equilibrium between Ti doping and surrounding S electrons at the Mo site. Contrastingly, in 2Ti-MoS_2, the Ti contribution to the electron decreases compared to 1Ti-MoS_2, resulting in an increase in electron donation from Mo. This phenomenon correlates with the observed change in Ti 3d states depicted in Fig. 2(f), where the overlap between Ti 3d and other energy levels near the Fermi level diminishes, thereby weakening electron transfer. In 3Ti-MoS_2, the Ti atom loses 0.96e of electrons. However, unlike 1Ti-MoS_2, electron gains and losses predominantly occur at the surface rather than achieving charge equilibrium with surrounding S atoms. Consequently, Mo atoms, which originally lost electrons, now gain electrons within the system. This phenomenon likely activates the surface active region, thereby facilitating the adsorption and conversion of gas molecules.

Besides, the bonding between different atoms inside MoS_2 before and after doping was investigated using Mulliken bond population calculations.[44] These calculations further quantify the extent of electron sharing between two atoms, providing deeper insights into the bonding characteristics.[45] It should be noted, however, that negative values for Mulliken bond populations are possible, indicating that the bond type is ionic and relatively easy to break if the absolute value is low.[46] Although Mulliken bond populations do not have a precise threshold value for distinguishing between ionic and covalent bonds, a bond with a Mulliken bond population greater than 0.1 is typically considered covalent, according to the literature.[47–49] Fig. 4 shows the calculated Mulliken bond populations for all models. Through calculations, it is observed that Mo and S exhibit distinct covalent bond characteristics. Similarly, in 1Ti-MoS_2 and 3Ti-MoS_2, Ti and S also form covalent bonds. However, the covalent bond characteristics in 2Ti-MoS_2 are significantly weakened. This result aligns with the lower overlap of Ti and Mo orbitals in the PDOS.

3.2 CO_2 adsorption on the Ti-doped MoS_2 monolayer

In order to analyze the optimal adsorption site of CO_2 on the surface, the geometric structure of the CO_2 was first optimized

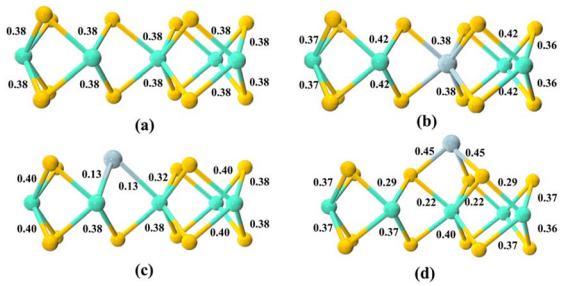

Fig. 4 The Mulliken bond populations for the: (a) MoS_2; (b) 1Ti-MoS_2; (c) 2Ti-MoS_2; (d) 3Ti-MoS_2.

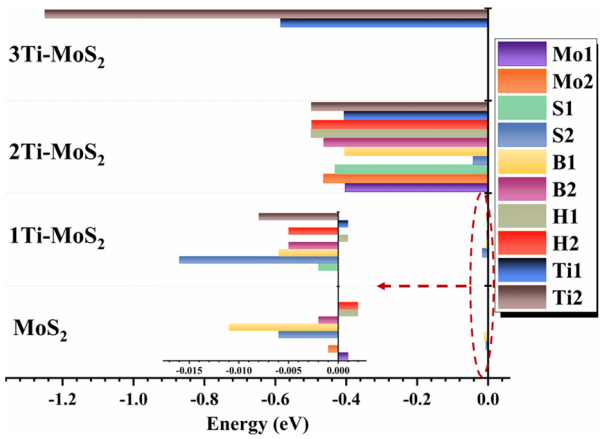

Fig. 5 The optimized energy of CO_2 adsorption on different site.

to its most stable configuration. The calculated C=O bond length was 1.172 Å, and the O=C=O bond angle was found to be 180°, which is in good agreement with the experimental data and previously derived theoretical values.[50]

Then the adsorption energy of CO_2 at different sites on the surface after optimization was calculated. The molecular height is defined as the minimum distance from any atom in the CO_2 molecule from any atom in the MoS_2. Four potential locations for CO_2 adsorption on the MoS_2 surface were identified: above a Mo atom (Mo site), above an S atom (S site), above a Ti atom (Ti site), above the center of a hexagon composed of three Mo atoms and three S atoms (Hollow site), and above a Mo–S bond (Bridge site). With a view to establish which of these are the most stable configuration for the CO_2 adsorption, two adsorption orientations (horizontal-1 and vertical-2) of the CO_2 molecule were also considered. Fig. 5 illustrates the CO_2 adsorption energy for all potential adsorption sites. Certain adsorption sites, not depicted in the figure, result from CO_2 relocating to

Table 3 The calculated Bader charge for all models

	Bader net atomic charge			
Atom type	MoS_2	1Ti-MoS_2	2Ti-MoS_2	3Ti-MoS_2
S	(−0.30) – (−0.35)	(−0.23) – (−0.54)	(−0.45) – (−0.68)	(−0.03) – (−1.00)
Mo	(0.65) – (0.66)	(0.51) – (1.10)	(0.75) – (1.12)	(−0.84) – (1.05)
Ti	*	1.00	0.62	0.96

other best adsorption sites during calculations. For simplicity, we only present the optimal adsorption sites.

Analyzing changes in adsorption energy at different sites reveals that pure MoS_2 exhibits the maximum adsorption energy of −0.011 eV for horizontal placed CO_2 at the bridge site. Meanwhile, MOS_2 and 1Ti-MOS_2, lacking effective Ti sites on the surface, exhibit minimal changes in adsorption energy. In some cases, the CO_2 adsorption energy at certain sites is positive, significantly impeding the adsorption process and hindering the catalytic conversion of CO_2. Furthermore, the adsorption energy of 2Ti-MoS_2 and 3Ti-MoS_2 increases at multiple sites, with vertically placed CO_2 displaying higher adsorption energy, indicating that the activation of oxygen atoms may be the key to CO_2 adsorption.

Fig. 6 depicts the optimal structure of the four models with the best adsorption energy. In Fig. 6(a), the relaxed structure of a CO_2 molecule adsorbed on pristine MoS_2 is shown. The calculated distance between CO_2 and MoS_2 is 3.544 Å. The length of the C=O bond in the adsorbed CO_2 measures 1.172 Å, similar to the C=O bond length in free CO_2, indicating that MoS_2 does not significantly affect the adsorbed CO_2.

This suggests a weak interaction between the CO_2 and MoS_2. Fig. 6(b–d) clearly shows a gradual decrease in the physical adsorption distance of CO_2, with the minimum adsorption distance between 3Ti-MoS_2 and CO_2 measuring 1.878 Å. This aligns with our predictions in Fig. 2 and 3, showing that 2Ti-MoS_2 and 3Ti-MoS_2 exhibit stronger adsorption capacity due to the additional electron cloud.

By further calculating adsorption energy, total charge, and the absolute values of the change in bond length/angle, we identified the adsorption changes of CO_2 on the surface, as presented in Table 4. Table 4 reveals that the E_{ads} value for CO_2 on pristine MoS_2 is 0.04 eV, consistent with the theoretically calculated value,[12] further indicating the limited CO_2 adsorption capacity of MoS_2. Additionally, the adsorption energy of 3Ti-MoS_2 is as high as −1.251 eV, suggesting a potential strong chemisorption reaction on the surface. The bond length of CO_2 in MoS_2 and 1Ti-MoS_2 remains unchanged, indicating ineffective activation of the surface C=O in the system. The absolute values of the change in the length of the C=O bond in CO_2 for 2Ti-MoS_2 exhibit a change of 0.013 Å, while the change for 3Ti-MoS_2 is twice that amount. Besides, similar conclusions are observed in the change of bond angle. The extra electrons and surplus active sites provided by Ti on the surface lead to significant distortion of C=O in 3Ti-MoS_2 ($\Delta\theta_{O=C=O}$=49.770°), enhancing surface catalytic performance. Considering the changes in C=O bond length and bond angle, both 2Ti-MoS_2 and 3Ti-MoS_2 demonstrate remarkable catalytic performance, with the activation performance of 3Ti-MoS_2 on CO_2 being more than 2 times higher than that of 2Ti-MoS_2.

Table 4 Characteristics of the most stable configurations of CO_2 adsorbed on MoS_2. (Δd1C–O and Δd2C–O represent the absolute values of the change in the length of the C=O bond in CO_2, respectively. $\theta_{O=C=O}$ is the O=C=O bond angle. $\Delta\theta_{O=C=O}$ is the absolute value of the change in the O=C=O angle from when the molecule is free)

Structure	E_{ads}, eV	Δd1C–O, Å	Δd2C–O, Å	$\theta_{O=C=O}$, °	$\Delta\theta_{O=C=O}$, °
MoS_2	−0.011	0	0	179.971	0.029
1Ti-MoS_2	−0.016	0	0	179.535	0.465
2Ti-MoS_2	−0.500	0.013	0.013	176.228	3.772
3Ti-MoS_2	−1.251	0.029	0.199	130.230	49.770

In order to further investigate the electron effect of different doped configuration on CO_2 adsorption, we also calculate the energy band and density state of all models. As shown in Fig. 7, comparing the structure of unadsorbed CO_2 model, it is found that the energy band and PDOS of pure MOS_2/CO_2 and 1Ti-MOS_2/CO_2 do not change significantly. The PDOS before and after CO_2 adsorption largely overlap, particularly in the region near the Fermi level. Consequently, the interaction between CO_2 and 1Ti-MoS_2 resembles the interaction between CO_2 and the pristine MoS_2.

Thus, we can infer that the interaction between CO_2 molecules and 1Ti-MoS_2 monolayers is weak, consistent with the calculated adsorption energy. The bandgaps of 2Ti-MOS_2/CO_2 and 3Ti-MOS_2/CO_2 undergo slight variations within a certain range after CO_2 adsorption, but the electronic transition types remain essentially unchanged.

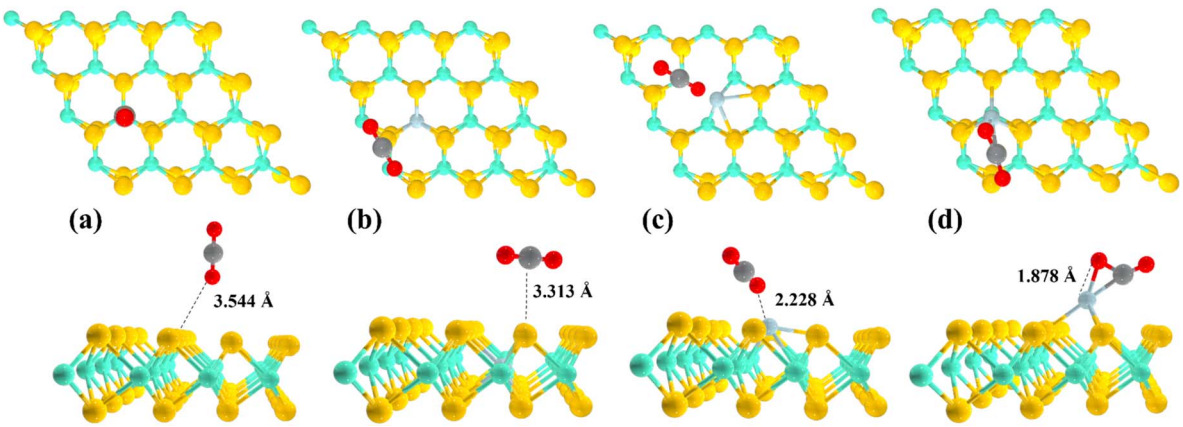

Fig. 6 The optimized structure of CO_2 adsorption on pristine MoS_2 (a), 1Ti-MoS_2 (b), 2Ti-MoS_2 (c), 3Ti-MoS_2 (d). The figure shows both plan (above) and side (below) views. The red and black ball in this paper represents O and C atoms, respectively. Dash line is the minimum distance from any atom in the CO_2 molecule from any atom in the MoS_2.

Besides, upon comparing the PDOS of different models in Fig. 7, it is evident that as the Ti doping site approaches the surface, the overall PDOS energy gradually shifts to the left. This characteristic is consistent with the unadsorbed structure.

Moreover, detailed comparisons of the changes in CO_2 1s state, CO_2 2p state, and Ti 3d state are depicted in Fig. 8. It is more evident from Fig. 8(a) that the orbitals of CO_2 and Ti do not significantly overlap, and the doping of Ti at the Mo site also does not affect the adsorption effect of CO_2. In Fig. 8(b), partial energy overlap is observed in the region above the 2–3 eV, and a faint overlap near −6 eV. These overlaps in state density confirm the increased adsorption energy of CO_2 on 2Ti-MoS_2. Simultaneously, Fig. 8(c) reveals a substantial decrease in the overall density of states compared to the previous model. This reduction in the electron state density of CO_2 suggests that the original C═O electron binding is influenced by Ti-doping. The diminished electron binding can weaken the double bond energy with lower energy, thereby increasing the availability of surface sites and facilitating the catalytic reaction. Furthermore, the overlapping range of the Ti 3d state and CO_2 electronic state near the Fermi level increases. This undoubtedly enhances the binding performance of Ti and CO_2, aligning with the calculated maximum adsorption energy.

In view of the above results, we also used electron differential charge density and Bader charge calculation to verify the charge

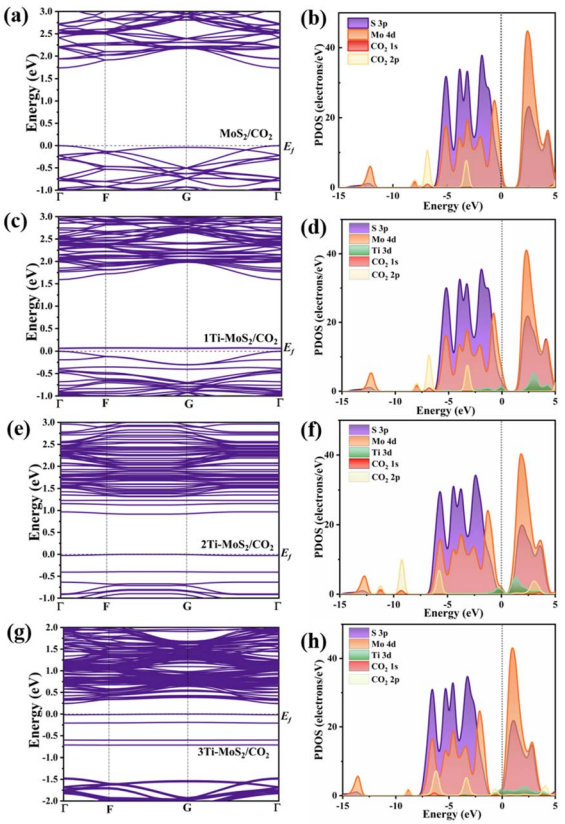

Fig. 7 Band structure and PDOS of (a and b) MoS_2/CO_2; (c and d) 1Ti-MoS_2/CO_2; (e and f) 2Ti-MoS_2/CO_2; (g and h) 3Ti-MoS_2/CO_2. The energy is referenced to the Fermi level (E_f), which is indicated by the dashed line at 0 eV.

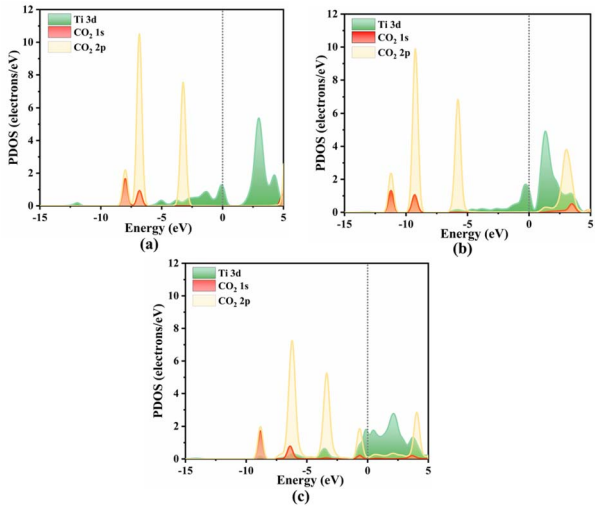

Fig. 8 The PDOS curves of (a) 1Ti-MoS_2; (b) 2Ti-MoS_2; (c) 3Ti-MoS_2. The dash lines are Fermi level. The energy is referenced to the Fermi level (E_f), which is indicated by the dashed line at 0 eV.

transfer between CO_2 and the catalyst, as shown in Fig. 9 and Table 5. Table 5 specifically presents the Bader net atomic charge of CO_2 and its closest atom. Where S_{near} represents the S atom closest to CO_2. Consistent with the previously calculated total charge results, the Bader net atomic charge sum of C and O in the remaining structures, except for the 3Ti-MoS_2 structure, remained relatively stable. This is also evident in Fig. 9, where

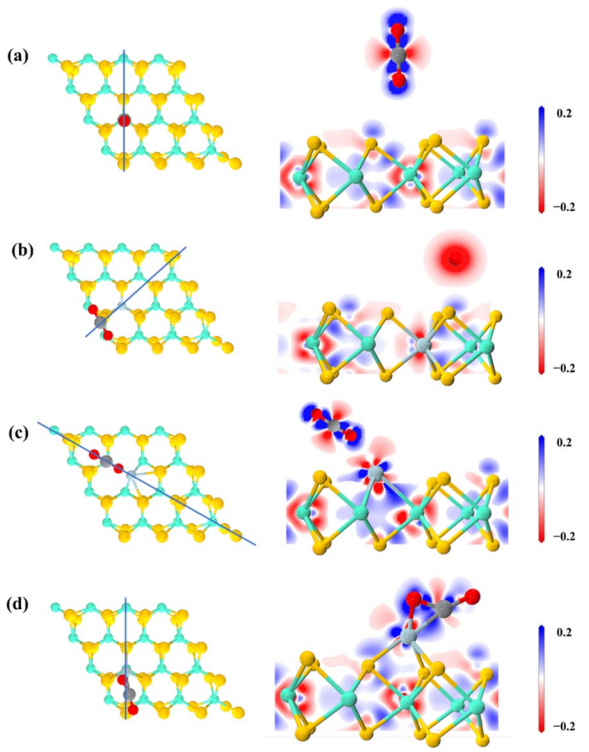

Fig. 9 The line in the figure represents the location of the slice of the electron density difference plot. (a) MoS_2/CO_2; (b) 1Ti-MoS_2/CO_2; (c) 2Ti-MoS_2/CO_2; (d) 3Ti-MoS_2/CO_2. The isovalue is set to 0.2 e $Å^{-3}$.

Table 5 The calculated Bader charge for all models

	Bader net atomic charge			
Atom type	MoS_2	1Ti-MoS_2	2Ti-MoS_2	3Ti-MoS_2
S_{near}	−0.50	−0.38	—	—
Ti	—	1.02	0.79	1.12
C	1.45	1.89	1.82	0.69
O1	−0.71	−0.96	−0.92	−0.67
O_2	−0.78	−0.96	−0.94	−0.90

only the CO_2 molecules in 2Ti-MoS_2 exhibit a slight change in adsorption among the first three catalysts. This, coupled with the electron density difference, substantiates the fact that its adsorption energy was heightened, leading to improved catalytic performance.

Despite Ti losing 1.02e, the gain and loss of these electrons remain stably coordinated with the surrounding S, considering its doping site is at the Mo site. As mentioned earlier, the optimal adsorption configuration of 2Ti-MoS_2 involves the vertical adsorption of Ti and O_2. Table 5 reveals that Ti loses 0.79e electrons, while O_2 gains a slightly larger number of electrons. This enhances the adsorption energy and involves a small amount of charge transfer. Furthermore, the Bader net atomic charge calculation for 3Ti-MoS_2 revealed that Ti lost more electrons, and C transferred fewer electrons to O. These findings confirm that Ti doping at this site significantly activates C=O, reducing energy in the adsorption process. In alignment with Fig. 9(d), an electron cloud structure formed between Ti and CO_2.

In addition, Mulliken bond populations of the adsorption model are also calculated, as shown in the Fig. 10. According to the calculation results, C=O presents a typical covalent double bond, and the calculated result is the same as the charge transfer observed in the MoS_2 and 1Ti-MoS_2 models, indicating that the bond type does not change. In the 2Ti-MoS_2 model, Ti and Mo tend to form ionic bonds, whereas in the 3Ti-MoS_2 model, both C and O atoms form covalent bonds with surface Ti atoms. These findings align well with the charge analysis results and suggest that Ti incorporation significantly enhances surface reactivity toward CO_2 adsorption. Such dopant-induced electronic reconstruction effectively activates the otherwise inert basal plane of MoS_2, providing a general strategy for designing 2D catalysts with tunable intrinsic activity beyond conventional edge or defect engineering.

3.3 The reaction mechanism of CO_2RR

Considering the importance of CO in CO_2RR over MoS_2, as observed in other experimental results,[25] we conducted further studies on the hydrogenation of intermediates *COOH and *CO to elucidate the underlying mechanisms. In order to comprehend the reaction mechanisms for the reduction of CO_2RR over MoS_2 and Ti/MoS_2, Fig. 9 illustrates the potential reaction pathways of CO_2RR based on previous DFT calculations.[22] Additionally, for the optimal reaction pathway, the following steps take place:

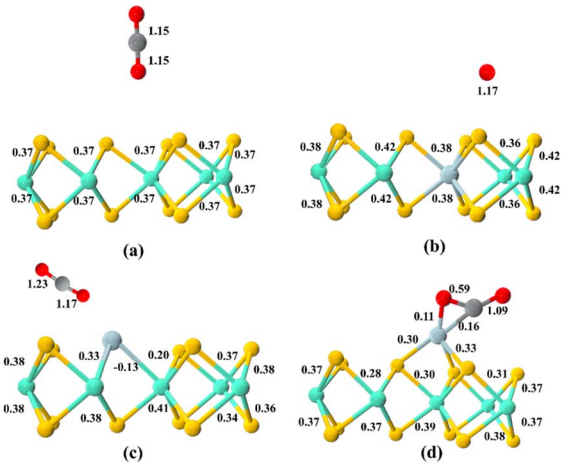

Fig. 10 The Mulliken bond populations for the: (a) MoS_2/CO_2; (b) 1Ti-MoS_2/CO_2; (c) 2Ti-MoS_2/CO_2; (d) 3Ti-MoS_2/CO_2.

$$CO_2 + * \rightarrow *CO_2 \quad (3)$$

$$*CO_2 + H* \rightarrow *COOH \quad (4)$$

$$*COOH + H* \rightarrow *CO + H_2O \quad (5)$$

Reaction step I involves the adsorption of CO_2, activating the CO_2 molecule. Step II encompasses the hydrogenation process of $*CO_2$, and the proposed reaction step III involves the hydrogenation of carboxyl (*COOH), leading to the reaction CO_2 → CO. As depicted in Fig. 9, the chemisorption of CO_2 on the surface lays the groundwork for subsequent reactions. Particularly evident in Fig. 11(b), the transition of CO_2 from the surface to the chemisorbed state reveals that the free energy barrier is lowest for 3Ti-MoS_2. This finding suggests that 3Ti-MoS_2 facilitates further adsorption reactions. Following CO_2 chemisorption, $*CO_2$ can undergo hydrogenation to form *COOH. However, the hydrogenation of $*CO_2$ to *COOH on pristine MoS_2 is found to be kinetically unfavorable, attributed to the high barrier energy of 3.046 eV, as shown in Fig. 11(b).

Our analysis of the energy profiles indicates that the $*CO_2$ → *COOH hydrogenation step represents the rate-determining step (RDS) for pristine MoS_2, 1Ti-MoS_2, and 2Ti-MoS_2 due to its high activation barrier. In contrast, the most active 3Ti-MoS_2 exhibits a markedly reduced barrier of only 0.177 eV for this step, effectively eliminating this kinetic limitation. As a result, the CO desorption step becomes the new RDS, with a relative barrier of 1.017 eV. This shift of the RDS clearly reflects a fundamental change in catalytic behavior induced by surface-exposed Ti dopants, highlighting the superior CO_2-to-CO conversion capability of 3Ti-MoS_2.

The introduction of the Ti coordination site on the basal plane significantly reduces the Gibbs free energy of the *COOH intermediate. It can be obviously found that Ti can effectively reduce the energy of the determination step under three different doping modes.

Compared with the electronic structure of Ti/MoS_2 as discussed before, the Ti doping on MoS_2 changes the band gap and charge, which favors strong adsorption of CO_2, resulting in

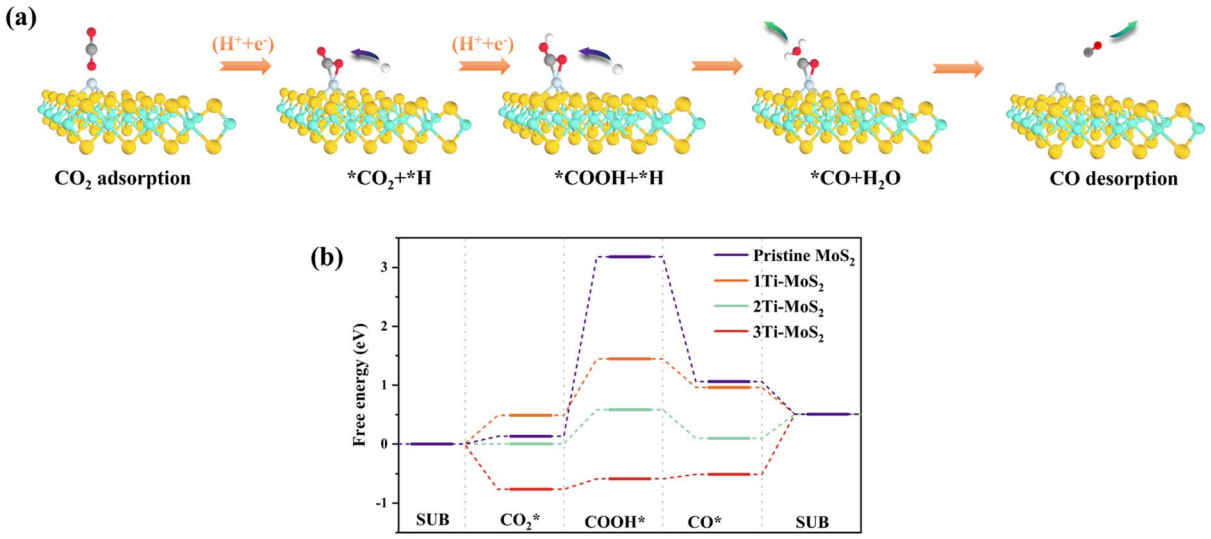

Fig. 11 The reaction mechanism for CO_2RR into CO on 3Ti-MoS_2. (a) The structures of the reaction intermediates; (b) the energy profile for different catalytic.

superior catalytic CO_2RR performance toward CO. Notably, 3Ti-MoS_2 exhibits exceptional catalytic performance with its *CO_2 to *COOH energy reduced to 0.177 eV, 17 times lower than that of pure MoS_2. Ultimately, the introduction of Ti enhances the desorption of CO, as evidenced by the calculated energy barrier for the CO desorption step on the surface. Both pure MoS_2 and 1Ti-MoS_2 surfaces exhibit intensified CO desorption processes, whereas 2Ti-MoS_2 and 3Ti-MoS_2 demonstrate notable energy barriers for the reaction. Notably, the energy barrier for CO desorption on the 3Ti-MoS_2 surface is particularly significant, reaching 1.017 eV. This suggests that the presence of *CO on this surface is conducive to further conversion processes. These theoretical trends are consistent with experimental observations[20,21,51] that MoS_2-based catalysts primarily yield CO as the dominant product in CO_2 reduction reactions, where moderate CO binding and reduced COOH activation barriers favor CO evolution.

Based on the energy calculations described above, a comparison is made among the formation energy, adsorption energy, adsorption barrier, determination step, and desorption barrier of various models, as illustrated in Fig. 12. It is worth noting that the formation energy of pure MoS_2 is merely used as a reference value of 0 eV and holds no practical significance in this context.

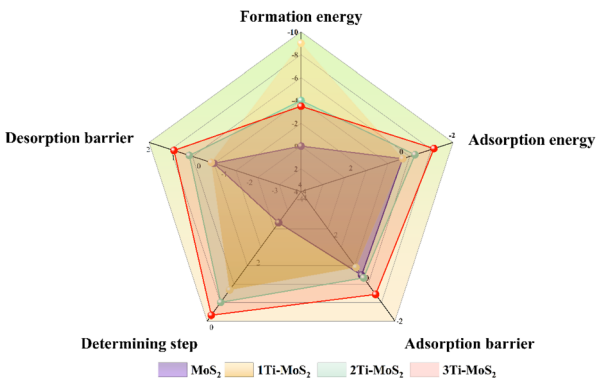

Fig. 12 Calculate each energy index diagram of the model.

Besides, the outstanding performance of the 3Ti-MoS_2 model pinpoints the surface-exposed Ti as the most potent active site design for CO_2RR, providing a valuable guiding principle for future catalyst development. The systematic theoretical analysis of the different doping sites offers valuable insight into future research on the TMD material, particularly in terms of assessing their overall CO_2RR performance. These results highlight a clear structure–property relationship between dopant configuration, charge redistribution, and catalytic activity, providing general design principles for developing efficient MoS_2-based single-atom catalysts that feature near-Fermi impurity levels and moderate charge transfer to optimize both adsorption and conversion steps.

Looking forward, the insights from this study offer clear pathways for experimental realization and application. The predicted thermodynamic stability of Ti in the MoS_2 lattice guides its synthesis *via* controlled hydrothermal or chemical vapor deposition methods.[52] Furthermore, the exceptionally low reaction barrier and high selectivity predicted for CO production position Ti/MoS_2 as a highly promising catalyst for CO_2 electrolyzers, motivating future work on fabricating and testing gas diffusion electrodes for high-current-density CO_2-to-CO conversion.

4 Conclusions

In conclusion, first principles quantum theory was employed to computationally screen M1/MoS_2 (M1 = Cr, Cu, Sc, Ti, V, and Ni) with the first series of transition metals. Ti/MoS_2 exerted a significant impact on the energy band structure, inducing changes in the band gap and electronic transition energy

through the introduction of impurity energy levels. Notably, the catalytic advantages of 3Ti-MoS_2 in CO_2 conversion were demonstrated through PDOS and electron density difference analysis. 3Ti-MoS_2 emerged as a potential material for CO_2 sensing due to its favorable adsorption and response characteristics. Furthermore, by calculating the reaction mechanism for CO_2RR into CO, we observed exceptional catalytic performance in 3Ti-MoS_2, with its *CO_2 to *COOH energy reduced to 0.177 eV, 17 times lower than that of pure MoS_2. These results highlight a clear structure–property relationship between dopant configuration, charge redistribution, and catalytic activity. The insights obtained here provide general design principles for developing efficient MoS_2-based single-atom catalysts, emphasizing dopants that introduce near-Fermi impurity levels and moderate charge transfer to optimize both adsorption and conversion steps.

Author contributions

Junbo Wang: conceptualization, investigation, methodology, visualization, software, writing–original draft. Qiankai Zhang: formal analysis, methodology, visualization, software, writing–original draft. Qi Tang: investigation, visualization, software, writing–original draft. Yin Zhang: methodology, visualization. Jun Zhou: writing–review & editing, project administration, supervision. Yang Wang: writing–review & editing, project administration, supervision. Kai Wu: supervision.

Conflicts of interest

There are no conflicts to declare.

Data availability

The data supporting the findings of this study are available within the article. No additional data were generated or analyzed in the presented research.

Supplementary information (SI): the optimized crystal structure data (in .cif format) supporting the computational findings of this study. The data is organized into three composite files: (1) 'All-Models_Clean-Structures' containing pristine and doped MoS_2 base models; (2) 'All-Models_with-CO_2' containing structures after CO_2 adsorption; and (3) 'All-Models_Step-Intermediates' containing the key reaction intermediate structures for all models. See DOI: https://doi.org/10.1039/d5ra08046k.

Acknowledgements

This research was funded by the Science and Technology Project of China Southern Power Grid Co., Ltd (Grant No. GDKJXM20231333), entitled "*Key Technology for Power-to-Gas Based on Coupled Co-electrolysis of $CO_2$and H_2O*".

References

1 M. Asadi, B. Kumar, A. Behranginia, B. A. Rosen, A. Baskin, N. Repnin, D. Pisasale, P. Phillips, W. Zhu, R. Haasch, *et al.*, Robust carbon dioxide reduction on molybdenum disulphide edges, *Nat. Commun.*, 2014, **5**, 4470.
2 S. Budinis, S. Krevor, N. M. Dowell, N. Brandon and A. Hawkes, An assessment of CCS costs, barriers and potential, *Energy Strategy Rev.*, 2018, **22**, 61–81.
3 L. Luo, M. Wang, Y. Cui, Z. Chen, J. Wu, Y. Cao, *et al.*, Surface iron species in palladium-iron intermetallic nanocrystals that promote and stabilize CO_2 methanation, *Angew. Chem., Int. Ed.*, 2020, **59**, 14434–14442.
4 Y. Yang, J. Liu, F. Liu and D. Wu, Reaction mechanism of CO_2 methanation over Rh/TiO_2 catalyst, *Fuel*, 2020, **276**, 118093.
5 M. Qiu, H. Tao, Y. Li, Y. Li, K. Ding, X. Huang, *et al.*, Toward improving CO_2 dissociation and conversion to methanol via CO-hydrogenation on Cu (100) surface by introducing embedded Co nanoclusters as promoters: a DFT study, *Appl. Surf. Sci.*, 2018, **427**, 837–847.
6 Z. Y. Sun, T. Ma, H. C. Tao, Q. Fan and B. X. Han, Fundamentals and challenges of electrochemical CO_2 reduction using two-dimensional materials, *Chem*, 2017, **3**, 560–587.
7 M. Chhowalla, H. S. Shin, G. Eda, L. J. Li, K. P. Loh and H. Zhang, The chemistry of two-dimensional layered transition metal dichalcogenide nanosheets, *Nat. Chem.*, 2013, **5**, 263–275.
8 X. Chia, A. Adriano, P. Lazar, Z. Sofer, J. Luxa and M. Pumera, Layered platinum dichalcogenides (PtS_2, $PtSe_2$, and $PtTe_2$) electrocatalysis: monotonic dependence on the chalcogen size, *Adv. Funct. Mater.*, 2016, **26**, 4306–4318.
9 H. Li, C. Tsai, A. L. Koh, L. Cai, A. W. Contryman, A. H. Fragapane, J. Zhao, H. S. Han, H. C. Manoharan, F. Abild-Pedersen, J. K. Norskov and X. Zheng, Activating and optimizing MoS_2 basal planes for hydrogen evolution through the formation of strained sulphur vacancies, *Nat. Mater.*, 2016, **15**, 48–53.
10 J. Liu, T. X. Liang, R. Tu, W. S. Lai and Y. J. Liu, Redistribution of π and σ electrons in boron-doped graphene from DFT investigation, *Appl. Surf. Sci.*, 2019, **481**, 344–352.
11 N. Yu, L. Wang, M. Li, X. Sun, T. Hou and Y. Li, Molybdenum disulfide as a highly efficient adsorbent for non-polar gases, *Phys. Chem. Chem. Phys.*, 2015, **17**, 11700–11704.
12 X. Mao, L. Wang, Y. Xu and Y. Li, Modulating the MoS_2 edge structures by doping transition metals for electrocatalytic CO_2 reduction, *J. Phys. Chem. C*, 2020, **124**, 10523–10529.
13 Z. Y. Li, D. A. Zhou and J. Xiangke, Highly selective adsorption on monolayer MoS_2 doped with Pt, Ag, Au and Pd and effect of strain engineering: A DFT study, *Sens. Actuators, A*, 2021, **332**, 113176.
14 J. Q. Xu, X. Li, W. Liu, Y. Sun, Z. Ju, T. Yao, C. Wang, H. Ju, J. Zhu, S. Wei, *et al.*, Carbon dioxide electroreduction into syngas boosted by a partially delocalized charge in

molybdenum sulfide selenide alloy monolayers, *Angew. Chem., Int. Ed.*, 2017, **56**, 9121–9125.
15 S. Park, J. Park, H. Abroshan, L. Zhang, J. K. Kim, J. M. Zhang, J. H. Guo, S. Siahrostami and X. L. Zheng, Enhancing catalytic activity of MoS_2 basal plane S-vacancy by Co cluster addition, *ACS Energy Lett.*, 2018, **3**, 2685–2693.
16 G. D. Shi, L. Yu, X. Ba, X. S. Zhang, J. Q. Zhou and Y. Yu, Copper nanoparticle interspersed MoS_2 nanoflowers with enhanced efficiency for CO_2 electrochemical reduction to fuel, *Dalton Trans.*, 2017, **46**, 10569–10577.
17 C. C. Wu, W. J. Yang, J. Y. Wang, R. Kannaiyan and I. D. Gates, CO_2 adsorption and dissociation on single and double iron atomic molybdenum disulfide catalysts: A DFT study, *Fuel*, 2021, **305**, 121547.
18 Q. Yu, Theoretical studies of non-noble metal single-atom catalyst Ni1/MoS_2: Electronic structure and electrocatalytic CO_2 reduction, *Sci. China Mater.*, 2022, **66**, 1079–1088.
19 B. Moss, Q. Wang, K. T. Butle, *et al.*, Linking in situ charge accumulation to electronic structure in doped $SrTiO_3$ reveals design principles for hydrogen-evolving photocatalysts, *Nat. Mater.*, 2021, **20**, 511–517.
20 V. S. Vaiss and L. T. Costa, Theoretical Systematic Investigation as a Strategic Tool for the Design of More Efficient Pure and Doped MoS_2 Catalysts for CO_2 Electroreduction, *Chem. Phys.*, 2025, **591**, 112597.
21 K. L. Lv, W. Q. Suo, M. D. Shao, Y. Zhu, X. P. Wang, J. J. Feng, M. W. Fang and Y. Zhu, Nitrogen doped MoS_2 and nitrogen doped carbon dots composite catalyst for electroreduction CO_2 to CO with high Faradaic efficiency, *Nano Energy*, 2019, **63**, 103834.
22 P. Abbasi, M. Asadi, C. Liu, S. Sharifi-Asl, B. Sayahpour, A. Behranginia, P. Zapol, R. Shahbazian-Yassar, L. A. Curtiss and A. Salehi-Khojin, Tailoring the edge structure of molybdenum disulfide toward electrocatalytic reduction of carbon dioxide, *ACS Nano*, 2017, **11**, 453–460.
23 J. W. Li, W. M. Jia, C. Liu, S. S. Lv, J. T. Wang and Z. C. Li, Static and dynamic evolution of CO adsorption on γ-U (1 0 0) surface with different levels of Mo doping using DFT and AIMD calculations, *Nucl. Sci. Tech.*, 2023, **34**, 142–154.
24 S. L. Yang, X. T. Wang, G. Lei, H. X. Xu, Z. Wang, J. Xiong and H. S. Gu, A DFT study on the outstanding hydrogen storage performance of the Ti-decorated MoS_2 monolayer, *Surf. Interfaces*, 2021, **26**, 101329.
25 Y. L. Xie, X. Li, Y. Wang, B. W. Li, L. Yang, N. Zhao, M. F. Liu, X. Z. Wang, Y. Yu and J. M. Liu, Reaction mechanisms for reduction of CO_2 to CO on monolayer MoS_2, *Appl. Surf. Sci.*, 2020, **499**, 143964.
26 Y. P. Miao, H. W. Bao, W. Fan, Y. Li and F. Ma, The adsorption behaviors of pristine MoS_2 and N-MoS_2 monolayer: A first-principles calculation, *Surf. Interfaces*, 2021, **27**, 101580.
27 S. J. Clark, M. D. Segall, C. J. Pickard, P. J. Hasnip, M. J. Probert, K. Refson and M. C. Payne, First principles methods using CASTEP, *Z. Kristallogr.*, 2005, **220**, 567–570.
28 J. P. Perdew, K. Burke and M. Ernzerhof, Generalized gradient approximation made simple, *Phys. Rev. Lett.*, 1996, **77**, 3865–3868.
29 H. Cui and P. F. Jia, Doping effect of small Rhn (n = 1–4) clusters on the geometric and electronic behaviors of MoS_2 monolayer: A first-principles study, *Appl. Surf. Sci.*, 2020, **526**, 146659.
30 C. P. Huelmo, M. G. Menezes, R. B. Capaz and P. A. Denis, Structural and magnetic properties of a defective graphene buffer layer grown on SiC(0001): a DFT study, *Phys. Chem. Chem. Phys.*, 2020, **22**, 19963–19972.
31 S. Grimme, Semiempirical GGA-type density functional constructed with a long-range dispersion correction, *J. Comput. Chem.*, 2006, **27**, 1787–1799.
32 C. Li, J. B. Li, F. M. Wu, S. S. Li, J. B. Xia and L. W. Wang, High capacity hydrogen storage in Ca decorated graphyne: A first-principles study, *J. Phys. Chem. C*, 2011, **115**, 23221–23225.
33 C. Freysoldt, B. Grabowski, T. Hickel, *et al.*, First-principles calculations for point defects in solids, *Rev. Mod. Phys.*, 2014, **86**, 253–305.
34 C. Z. He, R. Wang, D. Xiang, X. Y. Li, L. Fu, Z. Y. Jian, J. R. Huo and S. Li, Charge-regulated CO_2 capture capacity of metal atom embedded graphyne: a first-principles study, *Appl. Surf. Sci.*, 2020, **515**, 145392.
35 H. P. Zhan, A. J. Du, Q. B. Shi, Y. F. Zhou, Y. P. Zhang and Y. H. Tang, Adsorption behavior of CO_2 on pristine and doped phosphorenes: A dispersion corrected DFT study, *J. CO_2 Util.*, 2018, **24**, 463–470.
36 K. Ghosh, N. K. Mridha, A. A. Khan, N. Baildya, T. Dutta and K. Biswas, CO_2 activation on transition metal decorated graphene quantum dots: An insight from first principles, *Phys. E*, 2022, **135**, 114993.
37 M. Y. Wang, W. Wang, M. Ji and X. L. Cheng, Adsorption of phenol and hydrazine upon pristine and X-decorated (X = Sc, Ti, Cr and Mn) MoS_2 monolayer, *Appl. Surf. Sci.*, 2018, **439**, 350–363.
38 C. Ataca and S. Ciraci, Functionalization of single-layer MoS2 honeycomb structures, *J. Phys. Chem. C*, 2011, **115**, 13303–13311.
39 A. Abbasi, A. Abdelrasoul and J. J. Sardroodi, Adsorption of CO and NO molecules on Al, P and Si embedded MoS_2 nanosheets investigated by DFT calculations, *Adsorption*, 2019, **25**, 1493–1506.
40 A. Abbasi and J. J. Sardroodi, Theoretical study of the adsorption of NO_x on TiO_2/MoS_2 nanocomposites: a comparison between undoped and N-doped nanocomposites, *J. Nanostruct. Chem.*, 2016, **6**, 309–327.
41 R. Y. Zhang, D. Fu, J. M. Ni, C. B. Sun and S. X. Song, Adsorption for SO_2 gas molecules on B, N, P and Al doped MoS_2: the DFT study, *Chem. Phys. Lett.*, 2018, **712**, 51–58.
42 W. Huang, H. Da and G. Liang, Thermoelectric performance of MX2 (M=Mo, W; X=S, Se) monolayers, *J. Appl. Phys.*, 2013, **113**, 104304.
43 M. J. Szary, Adsorption of ethylene oxide on doped monolayers of MoS_2: A DFT study, *Mater. Sci. Eng., B*, 2021, **272**, 115341.
44 R. S. Mulliken, Electronic population analysis on LCAO–MO molecular wave functions. II. Overlap populations, bond

orders, and covalent bond energies, *J. Chem. Phys.*, 1955, **23**, 1841–1846.

45 Y. Wen, L. Wang, H. Liu and L. Song, Ab initio study of the elastic and mechanical properties of B19TiAl, *Crystals*, 2017, **7**, 39.

46 M. L. Ali, M. Khan, M. A. Al Asad, M. Z. Rahaman, M. Hasan, M. Chowdhury, M. K. Hossain, J. K. Modak, S. Ezzine and M. Amami, Highly efficient and stable lead-free cesium copper halide perovskites for optoelectronic applications: A DFT based study, *Heliyon*, 2023, **9**, e18816.

47 Y. Li, R. Wang, G. Zhu, G. Li and Y. Cao, A DFT study on the effect of lattice defects on the electronic structures and floatability of spodumene, *Phys. B*, 2024, **676**, 415657.

48 P. Barman, M. F. Rahman, M. R. Islam, M. Hasan, M. Chowdhury, M. K. Hossain, J. K. Modak, S. Ezzine and M. Amami, Lead-free novel perovskite Ba_3AsI_3: First-principles insights into its electrical, optical, and mechanical properties, *Heliyon*, 2023, **9**, e21675.

49 X. Wang, W. Liu, H. Duan, B. Wang, C. Han and D. Wei, The adsorption mechanism of calcium ion on quartz (101) surface: A DFT study, *Powder Technol.*, 2018, **329**, 158–166.

50 W. W. Cheng, Y. S. Xue, X. M. Luo and Y. Xu, A rare three-dimensional POM-based inorganic metal polymer bonded by CO_2 with high catalytic performance for CO_2 cycloaddition, *Chem. Commun.*, 2018, **54**, 1185–1188.

51 Y. Luo, Y. Xie, J. Zhou, Y. Li, Y. Yu and Z. Ren, Robust and Selective Electrochemical Reduction of CO_2: The Case of Integrated 3D TiO_2@MoS_2 Architectures and Ti–S Bonding Effects, *J. Mater. Chem. A*, 2018, **6**, 4706–4713.

52 J. Radhakrishnan and K. Biswas, Facile Synthesis of Ti Doped MoS_2 and Its Superior Adsorption Properties, *Mater. Lett.*, 2020, **280**, 128522.